Unconventional Quantum Hall Effect and Tunable Spin Hall Effect in Dirac Materials: Application to an Isolated MoS_{2} Trilayer

Xiao Li, Fan Zhang, and Qian Niu

Phys. Rev. Lett. **110**, 066803 — Published 5 February 2013

DOI: 10.1103/PhysRevLett.110.066803

Unconventional Quantum Hall Effect and Tunable Spin Hall Effect in MoS_2 Trilayers

Xiao Li,[1] Fan Zhang,[2,*] and Qian Niu[1]

[1] *Department of Physics, The University of Texas at Austin, Austin, Texas 78712, USA*
[2] *Department of Physics and Astronomy, University of Pennsylvania, Philadelphia, PA 19104, USA*

We analyze the Landau level (LL) structure in a MoS_2 trilayer and find a field-dependent unconventional Hall plateau sequence $\nu = \cdots -2M-6, -2M-4, -2M-2, -2M-1, \cdots, -5, -3, -1, 0, 2, 4 \cdots$. Due to orbital asymmetry, the low-energy Dirac fermions become heavily massive and the LL energies grow linearly with B, rather than with $\sqrt{B}$. Spin-orbital couplings break spin and valley degenerate LL's into two groups, with LL crossing effects present in the valence bands. In a p-n junction, spin-resolved fractionally quantized conductance appears in two-terminal measurements with a controllable spin-polarized current that can be probed at the interface. We also show the tunability of zero-field spin Hall conductivity.

PACS numbers: 73.43.-f, 71.70.Di, 72.25.Mk, 75.76.+j

Introduction.— Successful isolation of a single molybdenum disulfide (MoS_2) trilayer presents a new platform to explore interesting two dimensional (2D) electronic physics [1–4]. The honeycomb lattice structure of a MoS_2 trilayer (when viewed from the top) and its low-energy Dirac physics are reminiscent of graphene [5]. Indeed, the MoS_2 trilayer exhibits advantages over graphene in several areas of intense recent interest, specifically, whether this 2D material has an energy gap [6–8] and whether it has substantial spin-orbit couplings (SOC) [9–11]. Unfortunately, the answers for graphene to date are still not satisfactory, even though tremendous efforts have been made to improve the possibilities [12, 13].

When the layered compound MoS_2 is thinned down to a single trilayer, it departs from an indirect gap material to a direct gap material [2, 3, 14–17]. Additionally, some density functional theory (DFT) calculations have shown that there exists large SOC in MoS_2 [18–20]. The existence of a large energy gap and strong SOC may place this newly discovered 2D platform ahead of graphene in the race for the next generation of semiconductors. More recently a MoS_2 transistor with room-temperature mobility about $200\,\mathrm{cm}^2/(\mathrm{V{\cdot}s})$ has already appeared [4].

In this Letter, for the first time, we analyze how SOC influences the Landau level (LL) spectrum of massive Dirac fermions and how to increase the spin Hall effect in a MoS_2 trilayer. We find that the Hall plateau is field-dependent and follows an unconventional sequence that has an even–odd–even transition. The LL energies grow linearly with B, and the spin and valley degenerate LL's are broken into two groups with definite spin-valley couplings. The broken symmetry in the valence band also gives rise to LL crossing effects, leading to the enhancement of longitudinal magnetoresistance. We further investigate the case of a p-n junction, where spin-resolved fractionally quantized conductance appears in two-terminal measurements, with a controllable spin-polarized current that can be probed at the interface by STM. We also explicitly show how to tune and increase the zero-field spin Hall conductivity by reducing the inversion asymmetry. None of these unconventional band-structure effects has been observed in other Dirac fermion systems, even with the help of e-e interactions.

Continuum theory.— We start from a description of the low-energy model of an isolated MoS_2 trilayer, which applies generally to other group-VI dichalcogenides with the same crystal structure. The top and bottom S layers and the middle Mo layer are parallel triangular lattices. Because of their ABA relative stacking order, the top view of this trilayer forms a honeycomb lattice with S and Mo atoms at A and B sites, respectively. Near the Brillouin zone inequivalent corners K and K', the conduction and valence band states are approximately from $|\phi_c\rangle = |d_{z^2}\rangle$ and $|\phi_v^{\tau_z}\rangle = (|d_{x^2-y^2}\rangle + i\tau_z|d_{xy}\rangle)/\sqrt{2}$ orbitals, respectively. This effective two-band model has been suggested by DFT calculations [20] and supported by optical experiments [21–24]. To linear order in p, the effective $k{\cdot}p$ Hamiltonian in the above basis reads

$$\mathcal{H} = v(p_x\tau_z\sigma_x + p_y\sigma_y) + \Delta\sigma_z - \lambda\tau_z s_z\sigma_z + \lambda\tau_z s_z\,, \quad (1)$$

where the Pauli matrices $\boldsymbol{\sigma}$ operate on the space of the d_{z^2} and $d_{x^2-y^2}+id_{xy}$ orbitals, $\tau_z = \pm 1$ labels the K and K' valleys, and $s_z = \pm 1$ denotes the electron spin $\uparrow$ and $\downarrow$. The Fermi velocity v is $at/\hbar \sim 0.53\times 10^6\,\mathrm{m/s}$, where t is the effective hopping between the two Mo d-orbitals mediated by the S p-orbitals. As anticipated, the inversion asymmetry [25] between d_{z^2} and $d_{x^2-y^2}+id_{xy}$ orbitals gives rise to the $\Delta\sigma_z$ mass term which pins the ground state to a quantum valley Hall (QVH) insulator [26, 27]. Mo atoms provide strong intrinsic SOC $\sim \tau_z s_z\sigma_z$ [9, 27] that adjusts the energy gaps to $2(\Delta-\lambda)$ for $\tau_z s_z = 1$ bands and to $2(\Delta+\lambda)$ for $\tau_z s_z = -1$ bands. Note that this SOC perturbation preserves inversion ($\mathcal{P} = \tau_x\sigma_x$) [25] and time reversal ($\mathcal{T} = i\tau_x s_y K$) symmetries. As a combined effect of broken inversion symmetry and strong SOC, the term $\lambda\tau_z s_z$ breaks the particle-hole symmetry by oppositely shifting the $\tau_z s_z = \pm 1$ bands. Using $\Delta = 830\,\mathrm{meV}$ and $\lambda = 37.5\,\mathrm{meV}$ extracted from DFT calculations [20], Fig. 1 plots the band structure of a MoS_2 trilayer which exhibits two features that substantially dif-

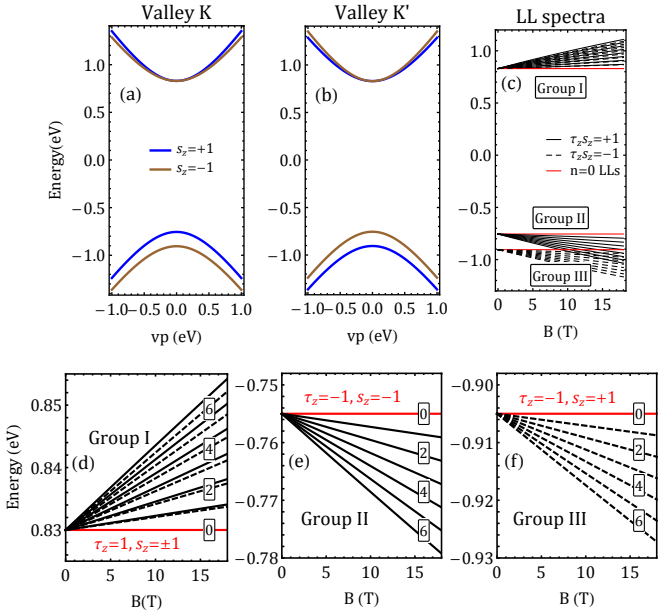

FIG. 1. (a) and (b) Electronic band structure near valley K and K'. (c) LL's with $n = 0, 10, ..., 80$ orbitals. (d)-(f) Enlarged view of the LL's in Group I, II, and III in (c). The $n \neq 0$ LL's are broken into $\tau_z s_z = 1$ doublets and $\tau_z s_z = -1$ doublets, due to the SOC and inversion asymmetry. LL crossing occurs between group II and III. The $n_{\rm I} = 0$ LL is spin degenerate and only appears at valley K. The $n_{\rm II}, n_{\rm III} = 0$ LL's are spin-filtered and appear only at valley K'.

fer from graphene, i.e., (i) a large QVH band gap and (ii) a lifted degeneracy between $\tau_z s_z = \pm 1$ bands. While the conduction band bottoms are lined up for all flavors, the valence band tops have a significant shift in energy between $\tau_z s_z = \pm 1$ bands. These symmetry breaking and spin-valley coupling can be further verified by the flavor-dependent energy dispersions

$$E_\pm = \lambda \tau_z s_z \pm \sqrt{v^2 p^2 + (\Delta - \lambda \tau_z s_z)^2}\,, \qquad (2)$$

where $\pm$ stands for the conduction and valence bands.

Broken symmetry LL's and LL crossing effects.— In the presence of a uniform perpendicular magnetic field, the 2D kinetic momentum $\boldsymbol{p}$ in Eq. (1) is replaced by $\boldsymbol{\pi} = \boldsymbol{p} + e\boldsymbol{A}/c$. In the Landau gauge $\boldsymbol{A} = (0, Bx)$, the operators $\pi = \pi_x + i\pi_y$ coincide with the lowering operators, satisfying $\pi\phi_n = -i(\hbar/\ell_B)\sqrt{2n}\phi_{n-1}$ and $\pi\phi_0 = 0$. Here $\ell_B = \sqrt{\hbar/(eB)} = 25.6/\sqrt{B[T]}$ nm is the magnetic length and ϕ_n is the nth LL eigenstate of an ordinary 2DEG. This model is approximately valid when $\hbar v/\ell_B$ is smaller than the band width ~ 300 meV. To focus on the influences from SOC and inversion asymmetry on the LL's, the relatively smaller effects including Zeeman couplings, disorders and Coulomb interactions are neglected [28]. We obtain the flavor-dependent LL spectrum

$$E_{n,\pm} = \lambda \tau_z s_z \pm \sqrt{n\hbar^2\omega_c^2 + (\Delta - \lambda \tau_z s_z)^2}\,, \qquad (3)$$

where $\omega_c = \sqrt{2}v/\ell_B$ is the cyclotron frequency. The corresponding eigenstates with $n > 0$ can be formally written as $(\phi_n, a^\pm_{n,s_z}\phi_{n-1})^T$ for valley K and $(b^\pm_{n,s_z}\phi_{n-1}, \phi_n)^T$ for K'. For $n = 0$ LL's, the eigenstates are $(\phi_0, 0)^T$ with energy Δ and $(0, \phi_0)^T$ with energy $-\Delta - 2\lambda s_z$. This shows that the $SU(4)$ invariant four anomalous $n = 0$ LL's are broken into a two-fold spin-degenerate conduction band $n_{\rm I} = 0$ LL at valley K and two spin-split valence band $n_{\rm II}, n_{\rm III} = 0$ LL's at K', as shown in Fig. 1(c), leading to quantum Hall effects at $\nu = 0$ and $\nu = -1$ but not $\nu = 1$. This is reminiscent of the anomalous $n = 0$ LL's in few-layer graphene systems [29]. In graphene the $SU(4)$ symmetry of $n = 0$ LL's are completely lifted by electron-electron interactions [30–32] while the particle-hole symmetry remains, whereas in the MoS_2 trilayer both the $SU(4)$ and particle-hole symmetries are broken by the intrinsic SOC and the inversion asymmetry.

Other unconventional LL features can be visualized in Fig. 1(c) and further understood by expanding Eq. (3) at $nB < 50$ T: $E_{n,\alpha} = (2\lambda\tau_z s_z \delta_{\alpha,-} + \alpha\Delta) + \frac{e\hbar v^2}{\Delta - \lambda\tau_z s_z} nB$ with $\alpha = \pm$. (i) Because of the heavily massive Dirac Fermion character, LL energies grow *linearly* with B, rather than with $\sqrt{B}$. (ii) SOC break the LL's into two groups with $\tau_z s_z = \pm 1$. However, each $n \neq 0$ LL is still doubly degenerate in each group, consisting of one spin $\uparrow$ state from one valley and one spin $\downarrow$ state from the other valley. (iii) The energies of two group LL's in the valence band not only have different slopes in B but also shift rigidly at $B = 0$, leading to LL crossing effects at

$$B_c = \frac{4\lambda(\lambda + \Delta)}{e\hbar v^2 (n_{\rm II} - n_{\rm III})} + \frac{8\lambda^2 n_{\rm III}}{e\hbar v^2 (n_{\rm II} - n_{\rm III})^2}\,, \qquad (4)$$

where $n_{\rm II}$ and $n_{\rm III}$ are the LL orbitals for Group II ($\tau_z s_z = 1$) and Group III ($\tau_z s_z = -1$) shown in Fig. 1(c).

As an example, in Fig. 2 we consider the crossings between LL's with $n_{\rm II} = 38, 39, 40, 41$ and LL's with $n_{\rm III} = 0, 1, 2$. The $n_{\rm III} = 0$ LL is non-degenerate while other LL's are all doubly degenerate. As a consequence, each region bounded by three LL's above the $n_{\rm III} = 0$ LL has an odd filling factor $\nu = -2(n_{\rm II} + n_{\rm III}) - 1$ while bounded by four LL's below has an even filling factor $\nu = -2(n_{\rm II} + n_{\rm III})$, where $n_{\rm II}$ and $n_{\rm III}$ are the orbital indices of the right and the lower LL's. In addition, the crossing points at the $n_{\rm III} = 0$ LL have degeneracy $g = 3$, while others all have $g = 4$. The crossing of two LL's results in increased degeneracies and lead to pronounced peaks in the measurement of longitudinal magnetoresistance. Unlike in other 2D materials, the LL crossing only occurs in the valence band of MoS_2 trilayer, reflecting the broken particle-hole symmetry by intrinsic SOC. This mechanism is distinct from the spin splitting in semiconductor quantum wells and the next-nearest interlayer hopping in ABA-stacked trilayer graphene [33].

Even in the absence of interactions, the Hall plateaus follow an unconventional sequence $\nu = \cdots, -2M - 6,$

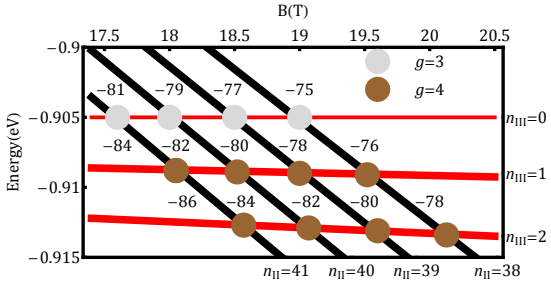

FIG. 2. The example of valence band LL crossing effect described in the text. All LL's are doubly degenerate except that the $n_{\rm III}=0$ LL is non-degenerate. The negative number denotes the filling factor of the region bounded by the surrounding LL's. The crossing points have degeneracy $g=3$ at $n_{\rm III}=0$ and $g=4$ otherwise.

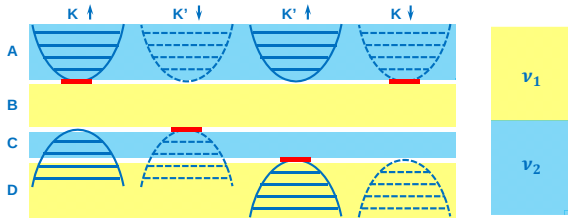

FIG. 3. Left panel: The solid (dashed) curves represent spin $\uparrow$ ($\downarrow$) bands and the parallel lines denote their LL's. Regions A-D are energy windows separated by the three lifted energies of the four $n=0$ LL's that are depicted by red lines. Right panel: a schematic p-n junction with two different filling factors ν_1 and ν_2 at two regions.

$-2M-4$, $-2M-2$, $-2M-1$, $\cdots$, -5, -3, -1, 0, 2, 4, $\cdots$, where $M=\left[4\lambda(\Delta+\lambda)/(eB\hbar v^2)\right]$ [34] reflects the fact that the $n_{\rm III}=0$ LL lies between the LL's with $n_{\rm II}=M$ and $n_{\rm II}=M+1$. The step of two in the sequence is a consequence of the $\tau_z s_z=\pm1$ classification, a hallmark of SOC. A step-one jump reflects the filling of a spin-filtered $n=0$ LL. The presence of $\nu=0$ and -1 arises from inversion asymmetry that makes Dirac fermions massive and from SOC that rigidly shifts the two groups of valence bands. The switching between even and odd filling factors is a direct result of broken $SU(4)$ symmetry among the anomalous $n=0$ LL's.

Spin-resolved p-n junctions.— A MoS_2 p-n junction can be realized by using electrostatic gating to locally control the carrier type and density in two adjacent regions. In such a device, transport measurements in the quantum Hall regime reveal new plateaus with integer and fractional filling factors of two-terminal conductance across the junction. This effect will arise from the redistribution of quantum Hall current among spin-resolved edge channels propagating along and across the junction, due to the presence of residue nonmagnetic disorder [35, 36]. When s_z is a good quantum number, because the edge channels of $n_{\rm II}, n_{\rm III}=0$ LL's are spin-filtered, the full equilibrium must be achieved within each spin species separately. Consequently, the net conductance (in units of e^2/h) across the junction is quantized as

$$G_{pp,nn}=\min\{|\nu_{1\uparrow}|,|\nu_{2\uparrow}|\}+\min\{|\nu_{1\downarrow}|,|\nu_{2\downarrow}|\}\,,$$
$$G_{pn}=\frac{|\nu_{1\uparrow}||\nu_{2\uparrow}|}{|\nu_{1\uparrow}|+|\nu_{2\uparrow}|}+\frac{|\nu_{1\downarrow}||\nu_{2\downarrow}|}{|\nu_{1\downarrow}|+|\nu_{2\downarrow}|}\,, \qquad (5)$$

where $\nu_{1\uparrow}+\nu_{1\downarrow}=\nu_1$ and $\nu_{2\uparrow}+\nu_{2\downarrow}=\nu_2$. In this limit, for a junction with $\nu_1=2n$ and $\nu_2=-1$, in the p-doped region the only available LL $n_{\rm II}=0$ is spin-filtered. Therefore, the net conductance is given by $G_{pn}=n/(n+1)$. This spin-resolved fractional quantization Eq.(5) has never been studied before. The conductance across the junction becomes spin-independent when s_z is not conserved, *e.g.*, due to magnetic disorders. This limit is similar to the case of graphene [37–39] where all possible filling factors are even numbers because of the spin degeneracy. Therefore, the net conductance reads $G_{pn}=|\nu_1||\nu_2|/(|\nu_1|+|\nu_2|)$ in the bipolar regime or $G_{pp,nn}=\min\{|\nu_1|,|\nu_2|\}$ in the unipolar regime. Take the same example with $\nu_1=2n$ and $\nu_2=-1$, G_{pn} in this spinless limit becomes $2n/(2n+1)$ instead.

In addition to the unconventional transport properties, STM probes at the interface can also detect a special fingerprint of the spin-filtered $n_{\rm II}=0$ LL. As shown in Fig. 3, when the Fermi energy of one region is fixed between the two valence band $n=0$ LL's (region C), namely, between $2\lambda-\Delta$ and $-2\lambda-\Delta$ indicated by Eq. (3), while the Fermi energy of the other is outside this energy window, there will be one spin-filtered chiral edge state, among all the $|\nu_1-\nu_2|$ channels, propagating along the interface. The chiral current will be *controllable* in the following senses. (i) Switching the magnetic field direction flips the spin-polarization of the current. (ii) Interchanging ν_1 and ν_2 switches the current direction while tuning ν_1 and ν_2 adjusts the current amplitude. (iii) Switching one of the Fermi level between A/B and D regions while fixing the other at C region changes the carrier type and flips the spin-polarization.

Spin Hall conductivity.— Clearly shown in Fig.3, the spin Hall conductivity is quantized to $\sigma_{SH}=e^2/h$ when the Fermi energy lies in the energy window C, due to the filling of spin-filtered $n_{\rm III}=0$ LL. We address that σ_{SH} does not vanish even in the absence of fields [40–43], which is another consequence of the nontrivial valence band structure of MoS_2 trilayers. In a massive Dirac fermion model, the Berry curvature [27, 44] in the valence band is nontrivial and reads

$$\Omega_{\hat{z}}(\boldsymbol{k},\tau_z,s_z)=\frac{\tau_z v^2 m}{2[v^2k^2+m^2]^{3/2}}\,, \qquad (6)$$

where $m=\Delta-\lambda\tau_z s_z$ is the flavor-dependent mass. At zero temperature, we obtain the valence band spin Hall conductivity by integrating $s_z\Omega_{\hat{z}}(\boldsymbol{k},\tau_z,s_z)$ over the occupied states and summing over the spin-valley flavors. As it happens in MoS_2 trilayers, the inversion asymmetry

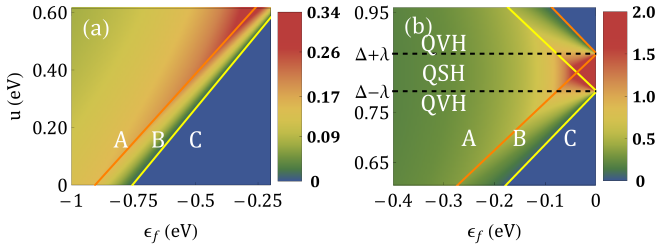

FIG. 4. (a) Valence band spin Hall conductivity $\sigma_{SH}(e^2/h)$ as a function of ϵ_f and u that reduces inversion asymmetry. The yellow (orange) line denotes the top of the $\tau_z s_z = +1\,(-1)$ valence band. (b) Quantum phase transitions between QVH and QSH states at $u = \Delta \pm \lambda$.

dominates the SOC ($\Delta > \lambda$) and the system is pinned to a QVH insulator in which $\sigma_{SH} = 0$ when the Fermi energy ϵ_f lies in the gap, implied by the τ_z dependence of $\Omega_{\hat{z}}$. Due to the mass difference between $\tau_z s_z = 1$ and $\tau_z s_z = -1$ groups, however, σ_{SH} contributions from the two groups are not completely canceled out when ϵ_f crosses valence bands. These features can be seen in the $u = 0$ line trace in Fig. 4(a). If in the opposite limit, assuming $\Delta = 0$, the system becomes a quantized spin Hall (QSH) insulator with $\sigma_{SH} = 2$ as shown by the middle zone in Fig. 4(b). Therefore, if the inversion asymmetry could be compensated externally, σ_{SH} will be enhanced as long as ϵ_f crosses the valence band, even though the system remains a QVH insulator. The inversion asymmetry arises from the difference between d_{z^2} and $d_{x^2-y^2} + id_{xy}$ orbitals, which can be possibly modulated by chemical doping, straining or electric gating the two S layers. To investigate the tunability of σ_{SH} by varying ϵ_f and by reducing inversion asymmetry, we propose a linearized phenomenological theory, i.e., the p-independent terms in Eq. (1) are replaced by

$$\mathcal{V}(\tau_z, s_z) = \lambda(1 - \frac{u}{\Delta})\tau_z s_z + (\Delta - u)\sigma_z - \lambda\tau_z s_z \sigma_z\,, \quad (7)$$

where u is the modeled potential that reduces the inversion asymmetry. In the limit of $u = 0$ this model recovers Eq. (1). In the special case of $u = \Delta$, inversion symmetry is restored and both σ_z and $\tau_z s_z$ terms vanish.

Fig. 4 plots σ_{SH} as a function of ϵ_f and u. The yellow (orange) line maps out where ϵ_f touches the top of the valence band with $\tau_z s_z = +1$ ($\tau_z s_z = -1$). In region C where ϵ_f is inside the bulk gap, σ_{SH} is identically 0. When ϵ_f lies between the two valence band tops (region B), σ_{SH} increases with decreasing ϵ_f. After ϵ_f drops far below the lower valence band top (region A), σ_{SH} starts to decrease slowly. Overall, σ_{SH} is maximized when ϵ_f is near the lower valence band top and grows substantially as u increases. When u is further increased, continuous quantum phase transitions (QVH-QSH-QVH) occur at $u = \Delta \mp \lambda$, as shown in Fig. 4(b). Near the first (second) critical point, the mass of the Dirac fermions with $\tau_z s_z = 1$ ($\tau_z s_z = -1$) changes sign and σ_{SH} jumps from 0 to 2 (2 to 0) when ϵ_f is inside the gap.

Discussions.— The Hall plateau in graphene follows the sequence $\nu = 4(n + 1/2)$, with $SU(4)$ symmetry breaking only in the case of high fields, weak disorders, and strong interactions [30–32]. In sharp contrast, the quantum Hall ferromagnetism in a MoS_2 trilayer arises naturally with no need for interactions. SOC and inversion asymmetry also imprint a single-particle signature on the LL spectrum: the broken symmetry of the $n = 0$ LL's with energies independent of the field strength. The unconventional Hall plateau sequence becomes even richer in a p-n junction with the appearance of spin-resolved fractionally quantized conductance. A controllable spin-polarized current materializes within this geometry and can be probed by STM at the interface. Unlike in other 2D materials [33], the LL crossing effects only occur in the valence bands of MoS_2 trilayer. These two valence bands, split by SOC, are also imbalanced in their contributions to σ_{SH} at zero field with hope for increasing σ_{SH} by reducing the gap. The coexistence of these remarkable band-structure effects makes the MoS_2 trilayer a charming material even in the absence of interactions. With improvements on its mobility, the MoS_2 trilayer system may realize as an alternative to graphene in fulfilling the desire for a gaped Dirac system with strong SOC, and we also anticipate observations of its unique Hall phenomena discovered in this Letter.

Acknowledgment. — We are indebted to R. Hegde, W. Bao, A. H. MacDonald, K. F. Mak, and Y. Yao for helpful discussions. X. L. and Q. N. are supported by DOE-DMSE (DE-FG03-02ER45958), NBRPC (2012CB-921300), NSFC (91121004), and the Welch Foundation (F-1255). F. Z. has been supported by DARPA under grant SPAWAR N66001-11-1-4110.

* E-mail: zhf@sas.upenn.edu

[1] K. S. Novoselov, D. Jiang, F. Schedin, *et al.* Proc. Natl Acad. Sci. USA **102**, 10451 (2005).
[2] A. Splendiani, L. Sun, Y. Zhang, *et al.* Nano Lett. **10**, 1271 (2010).
[3] K. F. Mak, C. Lee, J. Hone, J. Shan and T. F. Heinz, Phys. Rev. Lett. **105**, 136805 (2010).
[4] B. Radisavljevic, A. Radenovic, J. Brivio, V. Giacometti, and A. Kis, Nat. Nano. **6**, 147 (2011).
[5] A. H. Castro Neto, F. Guinea, N. M. R. Peres, K. S. Novoselov, and A. K. Geim, Rev. Mod. Phys. **81**, 109 (2009).
[6] A. Bostwick, F. Speck, T. Seyller, *et al.*, Science **328**, 999 (2010).
[7] D. A. Siegela, C. Parka, C. Hwang, *et al.*, Proc. Natl Acad. Sci. USA **108**, 11365 (2011).
[8] D. C. Elias, R. V. Gorbachev, A. S. Mayorov, *et al.*, Nat. Phys. **7**, 701 (2011).
[9] C. L. Kane, and E. J. Mele, Phys. Rev. Lett. **95**, 226801

(2005).
[10] H. Min, J. E. Hill, N. A. Sinitsyn, B. R. Sahu, L. Kleinman, and A. H. MacDonald, Phys. Rev. B **74**, 165310 (2006).
[11] Y. Yao, F. Ye, X. Qi, S. Zhang, and Z. Fang, Phys. Rev. B **75**, 041401(R) (2007).
[12] A. Varykhalov, J. Sanchez-Barriga, A. M. Shikin, *et al.*, Phys. Rev. Lett. **101**, 157601 (2008).
[13] C. Weeks, J. Hu, J. Alicea, M. Franz, and R. Q. Wu, Phys. Rev. X **1**, 021001 (2011).
[14] T. Li and G. GalliJ. Phys. Chem. C **111**, 16192 (2007).
[15] S. Lebègue and O. Eriksson, Phys. Rev. B **79**, 115409 (2009).
[16] S. W. Han, H. Kwon, S. K. Kim, *et al.* Phys. Rev. B **84**, 045409 (2011).
[17] A. Kuc, N. Zibouche, and T. Heine, Phys. Rev. B **83**, 245213 (2011).
[18] Z. Y. Zhu, Y. C. Cheng and U. Schwingenschlogl, Phy. Rev. B **84**, 153402 (2011).
[19] E. S. Kadantsev, and P. Hawrylak, Solid State Commun. **152**, 909 (2012).
[20] D. Xiao, G. Liu, W. Feng, X. Xu and W. Yao, Phys. Rev. Lett. **108**, 196802 (2012).
[21] T. Cao, G. Wang, W. Han, H. Ye, *et al.* Nat. Commun. **3**, 887 (2012).
[22] H. Zeng, J. Dai, W. Yao, D. Xiao, and X. Cui, eprint arXiv:1202.1592 (2012).
[23] K. F. Mak, K. He, J. Shan, T. F. Heinz, e-print arXiv:1205.1822 (2012).
[24] G. Sallen, L. Bouet, X. Marie, *et al.* e-print arXiv:1206.5128 (2012).
[25] Here the orbital inversion symmetry is analogous to the parity inversion symmetry in graphene. For a MoS_2 trilayer, this symmetry is only well defined in the low-energy model and is irrelevant in any lattice models.
[26] D. Xiao, W. Yao, and Q. Niu, Phys. Rev. Lett. **99**, 236809 (2007).
[27] F. Zhang, J. Jung, G. A. Fiete, Q. Niu, and A. H. MacDonald, Phys. Rev. Lett. **106**, 156801 (2011).
[28] The Zeeman coupling is at least one order of magnitude smaller than the cyclotron frequency.
[29] F. Zhang, D. Tilahun, and A. H. MacDonald, Phys. Rev. B **85**, 165139 (2012) and the references therein.
[30] J. G. Checkelsky, L. Li, and N. P. Ong, Phys. Rev. Lett. **100**, 206801 (2008).
[31] X. Du, I. Skachko, F. Duerr, A. Luican, and E. Y. Andrei, Nature **462**, 192 (2009).
[32] A. F. Young, C. R. Dean, and L. Wang, Nat. Phys. doi: 10.1038/nphys2307 (2012).
[33] T. Taychatanapat, K. Watanabe, T. Taniguchi and P. Jarillo-Herrero, Nat. Phys. **7**, 621 (2011).
[34] This sequence is general and shall be slightly modified at the LL crossing points. The analysis is similar to the example shown in Fig. 2. The function $[x]$ here takes the integer part of the argument x.
[35] P. Carmier, C. Lewenkopf, and D. Ullmo, Phys. Rev. B **81**, 241406(R) (2010).
[36] P. Carmier, C. Lewenkopf, and D. Ullmo, Phys. Rev. B **84**, 195428 (2011).
[37] J. R. Williams, L. DiCarlo, and C. M. Marcus, Science **317**, 638 (2007).
[38] D. A. Abanin, and L. S. Levitov, Science **317**, 641 (2007).
[39] B. Ozyilmaz, P. Jarillo-Herrero, D. Efetov, D. A. Abanin, L. S. Levitov, and P. Kim, Phys. Rev. Lett. **99**, 166804 (2007).
[40] S. Murakami, N. Nagaosa, and S. Zhang, Science **301**, 1348 (2003).
[41] J. Sinova, D. Culcer, Q. Niu, *et al.*, Phys. Rev. Letts. **92**, 126603 (2004).
[42] Y. K. Kato, R. C. Myers, A. C. Gossard, and D. D. Awschalom, Science **306**, 1910 (2004).
[43] N. Nagaosa, J. Sinova, S. Onoda, A. H. MacDonald, and N. P. Ong, Rev. Mod. Phys. **82**, 1539 (2010).
[44] D. Xiao, M. Chang, and Q. Niu, Rev. Mod. Phys. **82**, 1959 (2010).